I&EC research
Industrial & Engineering Chemistry Research
pubs.acs.org/IECR
Article

Comparison of Central Jet and Annular Sheet Atomizers at Identical Gas Momentum Flows

Simon Wachter,* Tobias Jakobs, and Thomas Kolb

Cite This: *Ind. Eng. Chem. Res.* 2021, 60, 11502−11512
Read Online
ACCESS | Metrics & More | Article Recommendations

ABSTRACT: This study compares three different nozzle flow configurations—central liquid jet with surrounding gas phase, liquid sheet with central gas phase, and liquid sheet with inner and outer gas phases. To guarantee constant velocities, as well as momentum flows at the nozzle orifice, a nozzle with identical orifice areas (a central tube with inner and outer slits) was utilized in the experiments. The influence of gas velocity (GLR), dynamic viscosity of the liquid, and nozzle configuration on the resulting droplet sizes (D_{32}, $ID_{32,m}$) and primary breakup was investigated at constant liquid mass flow. A high-speed camera (HSC) was used for the detection of primary breakup, whereas droplet size measurements were performed with a phase Doppler anemometer. The variation of nozzle configuration exhibited distinct influence on the resulting breakup morphology and droplet size. Especially, for atomizing high-viscosity liquids, application of sheet configurations led to smaller droplet sizes compared to liquid jet configuration.

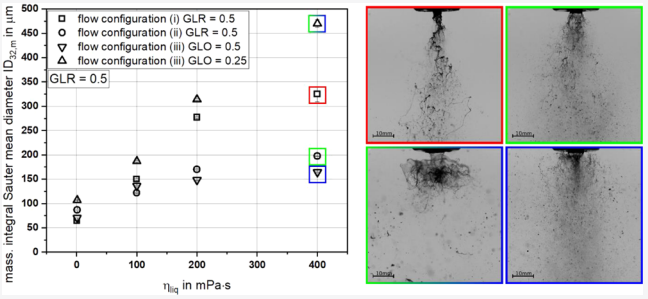

1. INTRODUCTION

Gas-assisted nozzles are applied to a wide field of applications in industrial processes. Beneath utilization in spray drying and gas cleaning, there are also applications in combustion and synthesis processes. This type of atomizer is available in several flow configurations: (i) central liquid jet and coaxial annular gas stream, (ii) annular liquid sheet with central gas jet, and (iii) annular liquid sheet with inner and outer gas stream. Each configuration can be utilized in energy-conversion systems, such as entrained flow gasifiers (EFGs). Here, biomass or waste-based feedstock are typically applied and feature high viscosities of up to 1000 mPa·s, as well as a complex rheological behavior. The feedstock are converted into syngas ($CO + H_2$), whereas oxygen serves as the gasification and atomization agent. As a result of the low stoichiometry required for the gasification reaction ($\lambda < 1$), the burner nozzle is typically operated at gas-to-liquid mass flow ratios of GLR < 1. Despite the large field of applications and the comparably simple atomizer geometry, there is still no fundamental understanding of the prevailing phenomena and physics.

For the optimization of the atomization process at conditions relevant to EFG, it is an essential research objective to gain deeper insights into the atomization process by applying various nozzle configurations and liquid properties. In particular, because of the fact that nozzles featuring central liquid jets reveal a limitation in disintegrating large liquid jet diameters, at increased liquid mass flow and low liquid velocity, the present work aims at investigating and comparing potentially scalable annular liquid sheet nozzles.

2. THEORETICAL BACKGROUND

The three different nozzle flow configurations under investigation are shown in Figure 1 as configurations (i−iii). Configuration (i) represents the central liquid jet configuration with an annular coaxial gas jet; (ii) illustrates an annular liquid sheet atomizer with a central gas jet; and (iii) is an annular

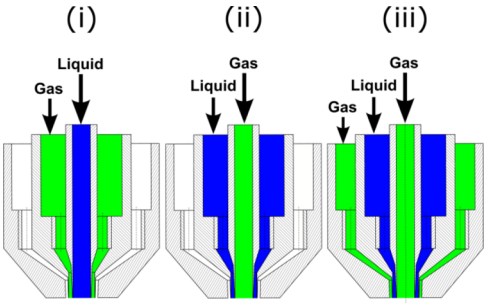

Figure 1. Schemes of the investigated nozzle flow configurations (i−iii).

Received: April 23, 2021
Revised: June 23, 2021
Accepted: June 25, 2021
Published: July 14, 2021

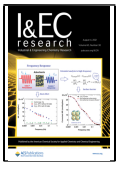

https://doi.org/10.1021/acs.iecr.1c01526
Ind. Eng. Chem. Res. 2021, 60, 11502−11512

liquid sheet atomizer with central and coaxial surrounding gas jet.

Faragò and Chigier performed detailed investigations of liquid jet breakup morphology, utilizing configuration (i) for air/water.[1] A classification for primary breakup was suggested for different atomizer geometries in terms of the jet diameter and gas orifice area by applying the liquid Reynolds number Re_{liq} and aerodynamic Weber number We_{aero}, according to eqs 1 and 2, to describe the jet breakup:

$$Re_{liq} = \frac{D_{liq} \times v_{liq} \times \rho_{liq}}{\eta_{liq}} \quad (1)$$

$$We_{aero} = \frac{D_{liq} \times (v_{gas} - v_{liq})^2 \times \rho_{gas}}{\sigma} \quad (2)$$

with liquid jet diameter D_{liq}, velocity v, density ρ, dynamic viscosity η, and surface tension σ. The subscripts *gas* and *liq* denote the gas and liquid phases, respectively. For constant Re_{liq}, the following representative spray conditions can be identified: the Rayleigh-type breakup (small We_{aero}), in which the liquid jet is fragmented into large droplets close to the spray center. With increasing We_{aero}, the membrane-type breakup is detected, with membranes near the nozzle orifice being generated and broken into small droplets. The accumulated rim of the membranes disintegrates into larger droplets, according to Rayleigh−Plateau instabilities. At high We_{aero}, the fiber-type regime is reached, which leads to a complete disintegration of the liquid jet into fibers near the nozzle orifice. The produced fibers disintegrate into small droplets according to the Rayleigh−Plateau instability. The fiber-type regime is divided into the submodes pulsating and superpulsating. Lasheras and Hopfinger[2] used the momentum flux ratio of gas and liquid phases j, according to eq 3, for characterizing the fiber-type breakup:

$$j = \frac{j_{gas}}{j_{liq}} = \frac{v_{gas}^2 \times \rho_{gas}}{v_{liq}^2 \times \rho_{liq}} \quad (3)$$

Zhao et al.[3] investigated the impact of dynamic viscosity on the primary breakup by applying suspensions in twin-fluid atomizers with a central liquid jet. In order to expand the regime classification concerning viscosity effects, the Ohnesorge number, which is in accordance with eq 4, was used. The breakup morphology was described by We_{aero} and Oh and was also classified into Rayleigh-type, fiber-type, and atomization.

$$Oh = \frac{\eta_{liq}}{\sqrt{D_{liq} \times \sigma \times \rho_{liq}}} \quad (4)$$

For the liquid-jet annular gas stream configuration, a large number of studies on the atomization of low-viscosity liquids (η_{liq} < 50 mPa·s) can be found in the literature.[4−8] A summary of the publications featuring η_{liq} > 50 mPa·s was presented by Wachter et al.[9] The dynamic viscosity was varied in the range of η_{liq} = 1−805 mPa·s. In general, an increase in the droplet diameter with increasing viscosity was reported.[8,10−13] This effect was explained by the damping effects of the liquid on the formation of instabilities. Furthermore, the dependency of the resulting droplet size on the spray morphology was demonstrated by Sänger,[14] who subdivided the proposed droplet size correlation into membrane-type and fiber-type regimes.

The second flow configuration (ii) provides the liquid as the annular sheet, whereas the gas stream emerges from the central tube. Investigations of the atomization of water with this nozzle configuration were performed by Leboucher et al.[15] and Zhao et al.,[16] who presented different diagrams for morphological classification. Both authors detected the bubble and Christmas-tree breakup regime. As the bubble regime occurs for low gas velocities and leads to gas-filled bubbles with liquid impingement,[17] the Christmas-tree breakup at an increased gas velocity creates a pulsating sheet that breaks into droplets. This breakup regime was further divided by Choi et al.[18] into the aerodynamic force-dominant and hydrodynamic force-dominant modes. Leboucher et al.[15] classified the regimes with gas and liquid momentum flow J_{gas} and J_{liq}, whereas Zhao et al.[16] used $We_{aero,sheet}$, see eq 5, and a dimensionless geometry ratio of sheet thickness-to-diameter of the entire liquid orifice.

$$We_{aero,sheet} = \frac{s_{liq} \times (v_{gas} - v_{liq})^2 \times \rho_{gas}}{\sigma} \quad (5)$$

Here, s_{liq} represents the liquid sheet thickness. For increased liquid sheet thickness, a fiber-type regime was detected, leading to a sheet disintegration with small fibers in the perpendicular direction to the sheet. Li et al. performed droplet size measurements, applying this nozzle configuration at v_{gas} > 180 m·s^{-1}.[19] As a result, a V-shaped radial Sauter mean diameter D_{32} profile was detected with a phase Doppler anemometer (PDA). For a significant increase in gas velocity, only a small decrease in the droplet size across the entire spray cone was detected. Leboucher et al.[15] presented results for different system pressures and gas swirl configurations. Radial profiles of the droplet diameter are only shown for the swirl variation, exhibiting a nearly constant droplet size for a wide range of swirl ratios.

Flow configuration (iii) has a liquid annular sheet, with two gas streams emerging, one from the central tube and one from the coaxial outer annular gap around the liquid sheet. Carvalho et al.[20] employed a high-speed camera (HSC) to investigate nozzles with this flow configuration with angled outer gas atomizing water. In the experiments v_{liq}, $v_{gas,i}$, $v_{gas,o}$, the liquid sheet thickness as well as the gas swirl ratio were varied, whereas the index i and o represent the inner and outer gas orifices, respectively. The inner gas stream velocity was varied up to $v_{gas,i}$ = 200 m·s^{-1} and was identified as being more relevant for the breakup of the liquid sheet. In contrast, the outer gas stream only led to a slight decrease in the primary breakup length. Nevertheless, the outer gas velocity was only increased up to $v_{gas,o}$ = 40 m·s^{-1}. The primary breakup length was also decreased when the swirl was added to the outer gas stream. For increasing the liquid sheet thickness, an increase in the primary breakup length was detected. Wahono et al.[21] also used a HSC to investigate the primary breakup of an atomizer with flow configuration (iii) that featured parallel exiting channels. The authors observed an amplified Kelvin−Helmholtz surface wave on the liquid sheet during primary breakup, which caused the rupture of the sheet into ligaments. The breakup was mainly dependent on the momentum flow ratios J_i and J_o for the respective gas flow (eqs 6 and 7), as well as the entire gas momentum flow (eq 8). Only for J_o, a dependency on the breakup frequency of the liquid sheet was discovered.

https://doi.org/10.1021/acs.iecr.1c01526
Ind. Eng. Chem. Res. 2021, 60, 11502−11512

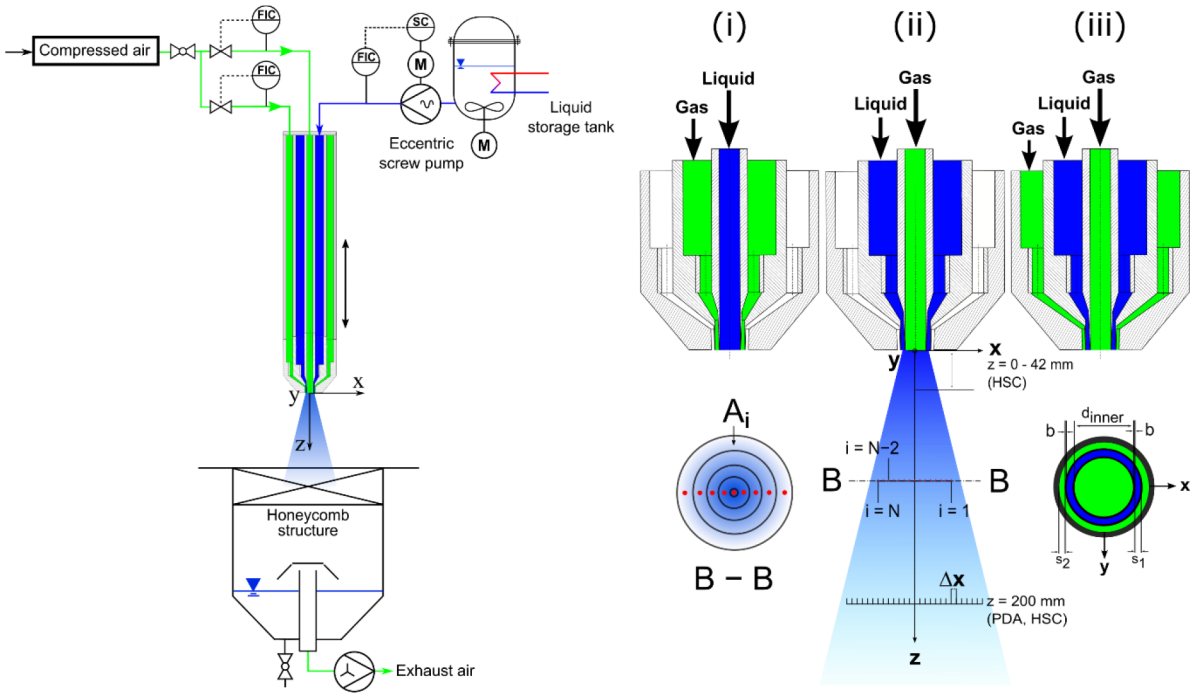

Figure 2. Schematic of the experimental setup applying nozzle configuration (iii), atmospheric spray test rig (ATMO) (left); schematic of the nozzle geometry applying the three investigated configurations (right).

$$J_i = \frac{J_{gas,i}}{J_{liq}} = \frac{v_{gas,i}^2 \times \rho_{gas} \times A_{gas,i}}{v_{liq}^2 \cdot \rho_{liq} \cdot A_{liq}} \quad (6)$$

$$J_o = \frac{J_{gas,o}}{J_{liq}} = \frac{v_{gas,o}^2 \times \rho_{gas} \times A_{gas,o}}{v_{liq}^2 \times \rho_{liq} \times A_{liq}} \quad (7)$$

$$J_{gas} = J_{gas,i} + J_{gas,o} \quad (8)$$

Duke et al.[22,23] performed an instability analysis for a nozzle with flow configuration (iii) and noted two physical instabilities: the Kelvin–Helmholtz instability (shear layer) and a nonlinear rupturing instability. As observed by Duke et al.,[22] the primary Kelvin–Helmholtz instability is only formed in the presence of a sufficiently high relative velocity of the outer gas stream $v_{gas,o}$ and liquid sheet v_{liq}. The required relative velocity was Δv = 30 m·s^{-1}. Further theoretical investigations of the liquid sheet breakup were performed by Cao et al.,[24] Ibrahim et al.,[25] and Lee et al.[26] In these studies, linear instability analyses were performed, with the researchers coming to the conclusion that the inner gas jet exhibits higher efficiency in terms of atomization compared to the outer gas stream. In addition to the investigation of instabilities, a scaling analysis was performed. As a result, the liquid sheet thickness showed a dominant effect on the resulting spray characteristics, as reported by Duke et al.[27]

The first PDA measurements of nozzles with flow configuration (iii) were performed by Leboucher et al.,[28] who applied water/air with different swirl configurations. This investigation demonstrated that the inner gas jet is more effective than the outer gas stream in terms of reducing droplet size. It should be noted that in this investigation, the maximum velocity of the outer gas stream was $v_{gas,o}$ = 90 m·s^{-1}, whereas the inner gas stream velocity was increased up to $v_{gas,i}$ = 180 m·s^{-1}, which could be a reason for the dominating effect of the inner gas stream compared to the outer one. Zhao et al.[29] used this flow configuration to perform laser diffraction measurements with water/air. Varying the exiting gas velocities, a maximum droplet diameter was detected when the outer gas jet was around $v_{gas,o}$ = 30–40 m·s^{-1}, which is independent of the inner gas velocities. Zhao et al.[29] assumed that the outer gas jet increases the velocity of the liquid phase, without disintegrating the liquid sheet, leading to a lower relative velocity between the liquid phase and the central gas stream, which dominated the atomization.

To summarize the literature overview, especially for atomizers in configuration (iii), the influence of the inner versus outer gas jet velocities or momentum flow ratios was not finally clarified. Nevertheless, the gas orifice area was not kept constant in previous experiments, leading to different dependencies of gas velocity on GLR, which results in varying gas momentum flows.

In order to overcome this effect, in the experiments described in this study, a nozzle with identical orifice areas (central tube/inner slit/outer slit) was used. The atomizer was operated in the previously outlined configurations (i), (ii), and (iii), which allows for their comparison at constant momentum flow ratios. Water and three different liquids with increasing viscosities were atomized at varying gas momentum flows. The resulting droplet size measurements and primary jet/sheet breakup detection were performed by means of a PDA and a HSC.

3. EXPERIMENTAL SETUP

The experiments were performed at the ATMOspheric spray test rig (ATMO), which is described by Wachter et al.[30] and depicted in Figure 2. A PDA system and a HSC were applied for spray investigations. The three-fluid lance was supplied with liquid using a pump and controlled via a Coriolis mass flow and density meter. A stirred and tempered liquid tank was

https://doi.org/10.1021/acs.iecr.1c01526
Ind. Eng. Chem. Res. 2021, 60, 11502–11512

applied in order to avoid temperature deviations. Two hot wire anemometers with valves were used to control the atomizing air mass flow. To avoid recirculation of small droplets, a high-power suction system was applied to the exhaust air; additionally, a honeycomb structure was placed at the inlet of the collection tank in order to serve as a flow straightener. The fittings at the top of the three-fluid lance were constructed in an identical manner to enable changes in the gas and liquid flow configurations between each channel of the lance and the nozzle-exiting position, respectively. The atomizer has a central tube with d_{inner} = 5.4 mm and two surrounding slits of s_1 = 1.09 mm and s_2 = 0.83 mm. In order to guarantee for constant velocities at the nozzle orifice, independent of the chosen flow configuration, all orifice areas were manufactured equal in size. The thicknesses of the tubes separating the flow at the nozzle orifice are reduced to b = 0.1 mm, which results in an undisturbed gas flow according to Tian et al.[31] The nozzle features parallel flow channels to enable the experimental results to be compared with other investigation results, such as those of Faragò and Chigier,[1] Zhao et al.,[16] and Wahono et al.[21]

For the variation of dynamic viscosity, water and three different glycerol/water mixtures were used. Surface tension and density of the four liquids applied were almost constant (see Table 1). The dynamic viscosity of the liquid phase was measured using a Physica MCR 101 rheometer from Anton Paar in Searle-type configuration.[32] Surface tension and density were determined using an EasyDyne tensiometer from Krüss, via the Du Noüy ring[33] and weighing methods. Relevant values of all liquids are presented in Table 1 for 20 °C and 1 atm.

Table 1. Physical Properties of All Applied Liquids at 20 °C and 1 atm

	η_{liq} in mPa·s	σ in N·m^{-1}	ρ_{liq} in kg·m^{-3}	Oh
water	1	0.0719	998	0.0026
glycerol/water (84.3 wt %)	100	0.0649	1220	0.2513
glycerol/water (89.5 wt %)	200	0.0642	1233	0.5027
glycerol/water (93.8 wt %)	400	0.0636	1244	1.0056

In the following paragraphs, only a short overview of the applied measurement systems is given. A detailed description is available in previous studies.[30,34,35]

A HSC (Photron SA4) was used for the detection of primary breakup. The setup was operated in backlight illumination with a 9 × 4500 lm high power light-emitting diode array. Sets of 2000 images were recorded for each operating point to ensure for a reliable data base.

At a distance of z = 200 mm, 10,000 images were taken, in order to (i) guarantee for optimal PDA settings; (ii) sphericity check the droplets in the measuring plane; (iii) qualitatively confirm tendencies measured by the PDA; and (iv) validation of PDA data in order to remove deviations according to the Gaussian beam effect.[36]

A fiber PDA with Spray Explorer by Dantec Dynamics was applied for the local investigation of droplet diameter and velocity. The system was operated in forward scattering arrangement (first-order refraction). Details of the settings are presented in Table 2. The settings of the system were optimized according to previous studies.[36,37] In this configuration, the maximum detectable droplet diameter is 1357 μm, as explained in a previous study.[38]

To guarantee for a high-quality data, a set of 50,000 droplets was taken at each measuring point. For some of the outermost measuring points, the sample size was not reached. However, minimum 10,000 droplets were measured at the spray boundary (x = ± 44 mm), ensuring statistical reliability, as reported in a previous study.[39] The toolbox *SprayCAT*[35] was used to compute arithmetic means as the mass-weighted integral Sauter mean diameter $ID_{32,m}$, according to eq 9.

$$ID_{32,m} = \frac{\sum_{i=1}^{N} D_{30,i}^{3} \dot{m}_i A_i}{\sum_{i=1}^{N} D_{20,i}^{2} \dot{m}_i A_i} \quad (9)$$

Detailed information concerning the calculation of the global size distribution and size moments is given by DIN SPEC 91325[40] and Albrecht.[38] The mass flux $\dot{m}_i$ was calculated from PDA data according to Albrecht.[38] All PDA measurements were performed at z = 200 mm distance from the nozzle orifice and repeated 3 times. For each operating point, the rotational symmetry of the measured profiles was checked, taking a full radial profile. Afterward, the repetition measurements were performed, taking half-profiles from the spray boundary to the center.

4. RESULTS AND DISCUSSION

In order to investigate the effect of the nozzle configuration on the resulting droplet size and primary breakup, nozzle configurations (i) and (ii) were compared at varying GLR (i.e., gas velocity v_{gas}) and dynamic viscosity η_{liq} at constant liquid mass flow of $\dot{M}_{liq}$ = 30 kg·h^{-1}. The atomization agent in all experiments was pressurized air at T = 20 °C. The supplied liquids were also tempered at T = 20 °C.

4.1. Comparison of Nozzle Configurations (i) and (ii) on the Droplet Size and Primary Breakup. For a comparison of nozzle configurations (i) and (ii), the operating conditions for both investigated parameters GLR and dynamic viscosity η_{liq} are presented in Table 3.

4.1.1. Influence of Nozzle Configurations (i) and (ii) on the Droplet Size and Primary Breakup at Varying GLR (i.e., v_{gas}) and Constant η_{liq} = 1 mPa·s. For a quantitative comparison of the two nozzle configurations, as well as for the description of the influence of GLR (v_{gas}) on the Sauter mean diameter, radial measurements were performed, as shown in Figure 3 (right).

Table 2. Settings of the PDA Evaluated by the Sensitivity Analysis

parameters	values	unit	parameters	values	unit
transmitter focal length f_T	1000	mm	laser wavelength λ_L	561	nm
receiver focal length f_R	1000	mm	laser power (transmitter exit)	40	mW
beam expander ratio E	1		off-axis angle Φ_R	70	°
receiver slit width (physical) l_S	200	μm	frequency shift f_Λ	80	MHz

https://doi.org/10.1021/acs.iecr.1c01526
Ind. Eng. Chem. Res. 2021, 60, 11502−11512

Table 3. Operating Conditions of the Experiments for the Comparison of Nozzle Configurations (i) and (ii) at a Constant Liquid Mass Flow of $\dot{M}_{liq}$ = 30 kg·h^{-1}

nozzle configuration	GLR in -	v_{gas} in m·s^{-1}	η_{liq} in mPa·s
(i)/(ii)	0.2	60	1
(i)/(ii)	0.3	90	1
(i)/(ii)	0.4	120	1
(i)/(ii)	0.5	150	1/100/200/400

The dependency of the Sauter mean diameter on GLR, for all measurements of (i) and (ii), the mass-weighted integral Sauter mean diameter $ID_{32,m}$ is shown in Figure 3 (left). As expected, with increasing GLR, for both nozzle configurations (i) and (ii), a decreasing Sauter mean diameter was measured. This effect results from an increase in the gas velocity (v_{gas} = 60 − 150 m·s^{-1}), which leads to higher aerodynamic forces that disintegrate the liquid jet or sheet. With increasing GLR, the influence on the resulting droplet size levels off. The influence of GLR on the resulting Sauter mean diameter, applying nozzle configuration (ii) at GLR > 0.4 (v_{gas} > 120 m·s^{-1}), is smaller compared to that using nozzle configuration (i).

In order to explain this effect, the radial Sauter mean diameter, for all measurements of (i) and (ii) is shown in Figure 3 (right). For GLR ≤ 0.3, the $ID_{32,m}$ is significantly lower for nozzle configuration (ii). In contrast to this, an increase above GLR > 0.4 leads to lower $ID_{32,m}$ values for configuration (i) (see Figure 3 (left)). For nozzle configuration (i), a W-shaped radial profile was detected, whereas configuration (ii) led to a V-shaped radial distribution, which is in accordance with the results of Li et al.[19] Typically, the flat W-shaped profile is achieved when the liquid jet is disintegrated by the high-velocity gas phase in the fiber-type breakup mode. As shown in Figure 4b), this mode leads to a slight increase in the droplet size at the spray center and a decrease at the spray boundary because of small, disintegrated fibers, leading to fine droplets following the gas phase. In this configuration, the liquid jet is fully disintegrated by the surrounding gas jet at high gas velocity. In contrast, the liquid sheet is already disintegrated into droplets for low gas velocities (see Figure 4c)), as against the liquid jet at the same gas velocity (see Figure 4a)). Applying configuration (ii) for increased gas velocity (see Figure 4d)), tiny droplets could be detected in the center of the spray, comparable to configuration (i), but larger droplets remained at the spray boundary without any further disintegration because of the lack of aerodynamic forces. As this breakup mode did not change with further increase in gas velocity and the droplet size at the spray boundary did not decrease, $ID_{32,m}$ exhibits only low sensitivity to GLR above GLR ≥ 0.4.

As can be seen in the HSC images, the spray angle differed significantly between nozzle configurations (i) and (ii). For configuration (i), the resulting jet fragments and droplets were accelerated in the axial direction, resulting in narrow spray angles. In contrast, the disintegration of the liquid sheet by the central gas stream at configuration (ii) led to a significant increase in the spray angle.

4.1.2. Influence of Nozzle Configurations (i) and (ii) on the Droplet Size and Primary Breakup at Varying Liquid Viscosities and Constant GLR = 0.5. To conduct a quantitative comparison of the two nozzle configurations (i) and (ii), as well as for the description of the influence of η_{liq} on the Sauter mean diameter, additional droplet size measurements were performed at an increased liquid viscosity of up to 400 mPa·s. The results are shown as $ID_{32,m}$ values in Figure 5.

As the measurements indicate, an increase in the droplet size could be detected for both nozzle configurations with increasing dynamic viscosity. This result had already been observed by many researchers, who typically applied flow configuration (i).[8,10−13] As damping effects of the liquid phase cause this effect, the same influence for increasing the liquid viscosity was expected for flow configuration (ii). However, configuration (ii) shows a minor influence of viscosity on the droplet size. As the application of configuration (i) led to a smaller droplet size of low-viscosity liquids (η_{liq} = 1 mPa·s), the droplet size results were already turned over for η_{liq} = 100 mPa·s. The same influence of viscosity and nozzle configuration was also apparent in the HSC images of the primary breakup, which are displayed in Figure 6.

Upon increasing the dynamic viscosity from η_{liq} = 1 mPa·s to η_{liq} = 400 mPa·s while applying nozzle configuration (i), the primary breakup significantly changed from the superpulsating fiber type, which resulted in a homogeneous spray with mostly

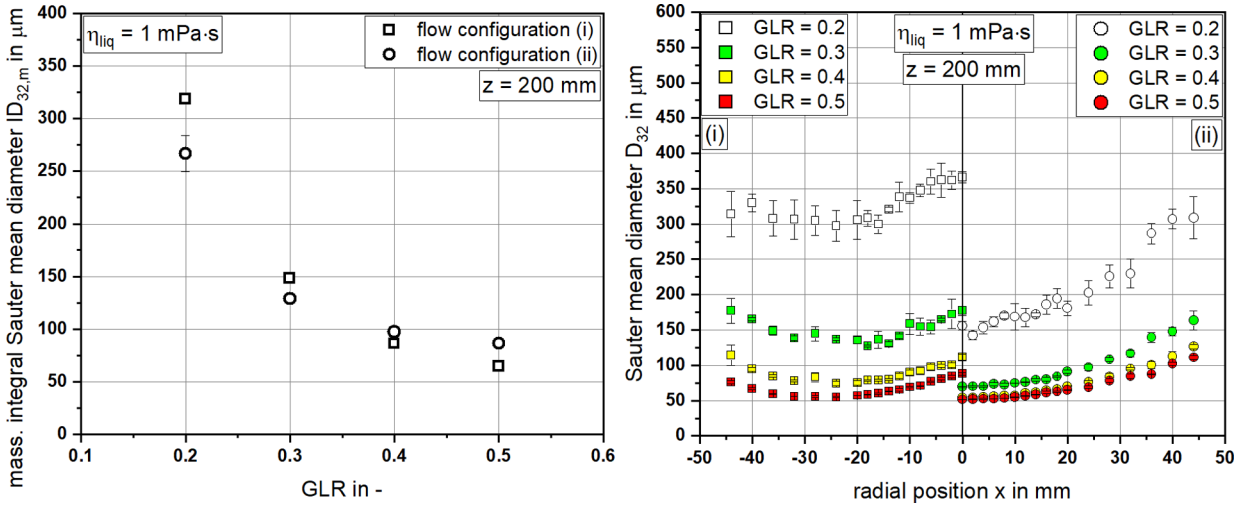

Figure 3. Resulting mass-weighted integral Sauter mean diameters (left) and radial measurements of the local Sauter mean diameter (right) using nozzle configurations (i) and (ii) at varying GLRs (i.e., v_{gas}) and constant dynamic viscosity η_{liq} = 1 mPa·s at z = 200 mm.

https://doi.org/10.1021/acs.iecr.1c01526
Ind. Eng. Chem. Res. 2021, 60, 11502−11512

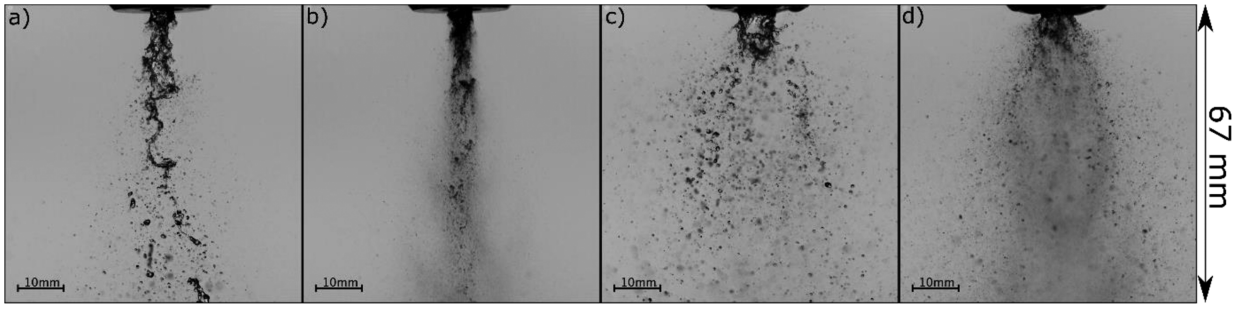

Figure 4. HSC images of the primary breakup of water (η_{liq} = 1 mPa·s) applying: (a) nozzle configuration (i) at GLR = 0.2 (v_{gas} = 60 m·s^{-1}); (b) nozzle configuration (i) at GLR = 0.5 (v_{gas} = 150 m·s^{-1}); (c) nozzle configuration (ii) at GLR = 0.2 (v_{gas} = 60 m·s^{-1}); and (d) nozzle configuration (ii) at GLR = 0.5 (v_{gas} = 150 m·s^{-1}).

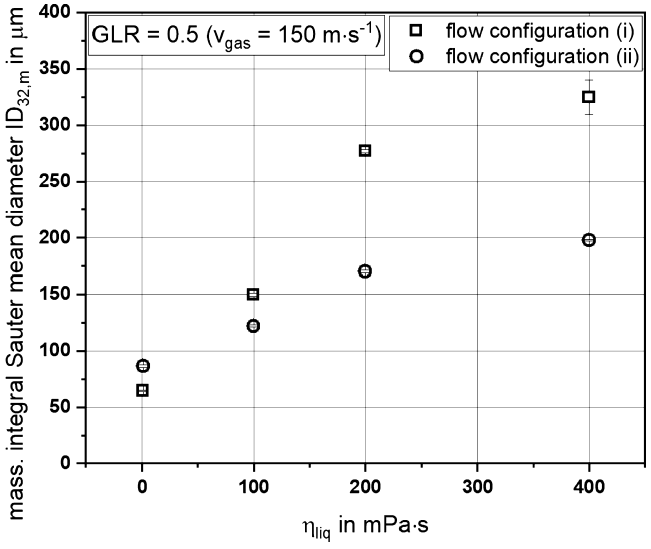

Figure 5. $ID_{32,m}$ measurements at constant GLR = 0.5 (v_{gas} = 150 m·s^{-1}) for nozzle configurations (i) and (ii) at varying dynamic viscosities.

very small droplets to the membrane-type breakup that revealed long ligaments and liquid fragments, along with an increased droplet size. In contrast, for nozzle configuration (ii), the breakup morphology did not significantly change with an increased liquid viscosity. Because of the fact that the emerging fuel sheet for configuration (ii) was thinner in size compared to the jet of configuration (i), almost no ligaments resulted from the primary breakup [even for the highest viscosity liquids (η_{liq} = 400 mPa·s) under investigation], leading to a smaller droplet size throughout the entire spray cone.

4.2. Extension of the Nozzle Geometry with the Outer Gas Gap to Configuration (iii). Being aware of the influence of the fast-flowing gas phase on the primary breakup and the resulting droplet size in terms of twin-fluid nozzles, an additional outer gas gap was employed in the liquid sheet configuration to reduce the increasing droplet size at the spray boundary shown in Figure 3. As fast gas phase emerges via two orifices, two mass flow ratios GLO and GLI were defined. GLO represents the mass flow ratio between the outer gas flow through the gas slit and liquid sheet, whereas GLI stands for the mass flow ratio between the inner gas flow through the central tube and liquid sheet. This definition yields the following equations:

$$\mathrm{GLR} = \mathrm{GLO} + \mathrm{GLI} \qquad \mathrm{GLO} = \frac{\dot{M}_{gas,o}}{\dot{M}_{liq}} \qquad \mathrm{GLI} = \frac{\dot{M}_{gas,i}}{\dot{M}_{liq}} \tag{10}$$

In an initial set of measurements, GLO (i.e., $v_{gas,o}$) and GLI (i.e., $v_{gas,i}$) were varied for constant GLR values at η_{liq} = 1 mPa·s. In addition, dynamic viscosity was investigated at GLR = 0.5 for GLO = 0, 0.25, and 0.5, resulting in $v_{gas,o}$ = 0, 75, and 150 m·s^{-1}. Thereafter, a comparison between nozzle configurations (i–iii) was performed for GLR = 0.5.

4.2.1. Influence of GLO/GLI on the Droplet Size and Primary Breakup Applying Nozzle Configuration (iii) at Constant Liquid Viscosity and Constant GLR = 0.3, 0.5, and 0.7. In order to compare the primary breakup and droplet size, nozzle configuration (iii) was applied at constant liquid viscosity η_{liq} = 1 mPa·s and GLR = 0.3, 0.5, and 0.7, but varying GLO and GLI. The measurements listed in Table 4 were performed. For a quantitative comparison of the resulting droplet sizes, the values for the $ID_{32,m}$ were used.

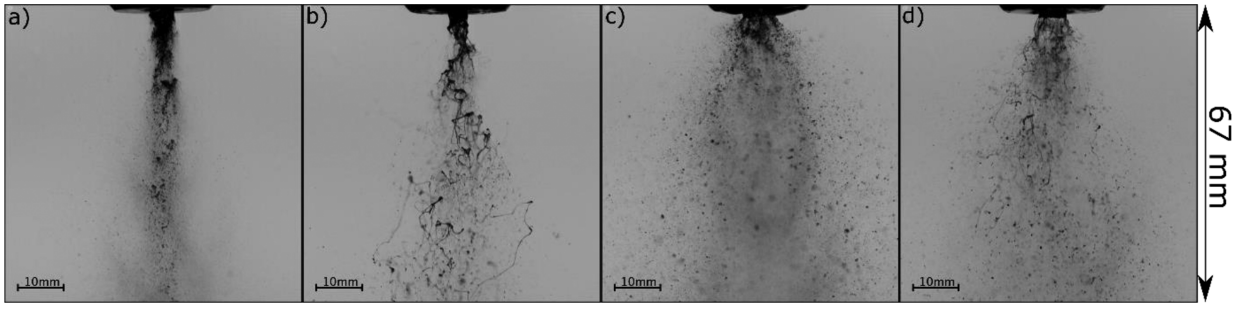

Figure 6. HSC images of the primary breakup at GLR = 0.5 (v_{gas} = 150 m·s^{-1}) applying (a) nozzle configuration (i) with η_{liq} = 1 mPa·s; (b) nozzle configuration (i) with η_{liq} = 400 mPa·s; (c) nozzle configuration (ii) with η_{liq} = 1 mPa·s; and (d) nozzle configuration (ii) with η_{liq} = 400 mPa·s.

https://doi.org/10.1021/acs.iecr.1c01526
Ind. Eng. Chem. Res. 2021, 60, 11502−11512

Table 4. Operating Conditions of the Experiments for Nozzle Configuration (iii) at a Constant Liquid Mass Flow of $\dot{M}_{liq}$ = 30 kg·h^{-1}, Liquid Viscosity of η_{liq} = 1 mPa·s, and GLR = 0.3, 0.5, and 0.7, but Varying GLI/GLO

GLR in -	GLO in -	GLI in -	$v_{gas,o}$ in m·s^{-1}	$v_{gas,i}$ in m·s^{-1}
0.3/0.5	0/0	0.3/0.5	0/0	90/150
0.3/0.5/0.7	0.06/0.1/0.14	0.24/0.4/0.56	18/30/42	72/120/168
0.3/0.5/0.7	0.12/0.2/0.28	0.18/0.3/0.42	36/60/84	54/90/126
0.3/0.5/0.7	0.15/0.25/0.35	0.15/0.25/0.35	45/75/105	45/75/105
0.3/0.5/0.7	0.18/0.3/0.42	0.12/0.2/0.28	54/90/126	36/60/84
0.3/0.5/0.7	0.24/0.4/0.56	0.06/0.1/0.14	72/120/168	18/30/42
0.3/0.5	0.3/0.5	0/0	90/150	0/0

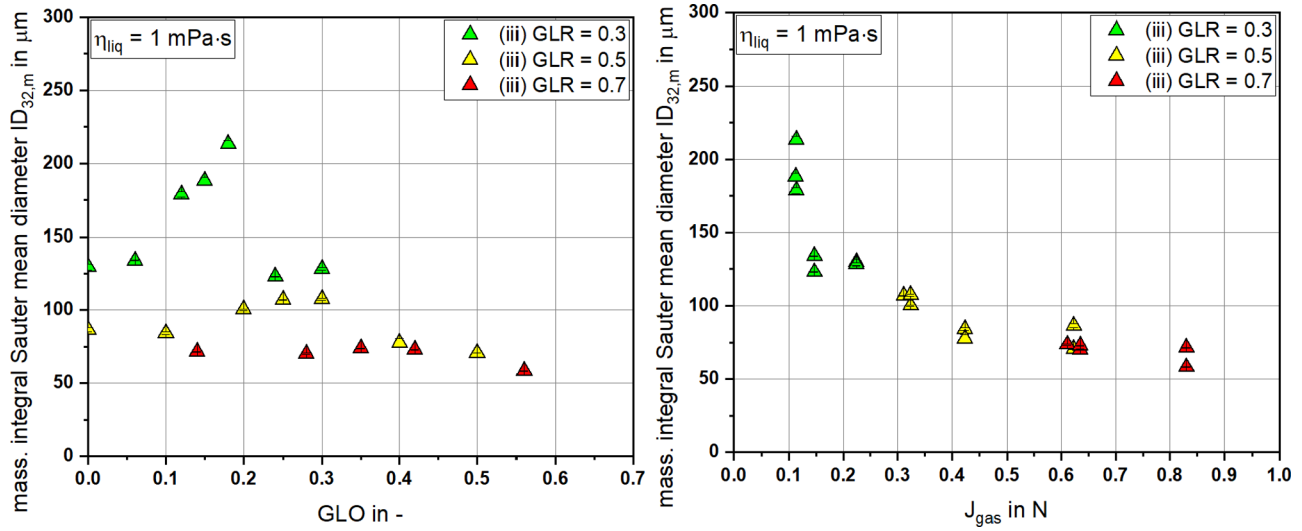

Figure 7. $ID_{32,m}$ measurements applying nozzle configuration (iii) at constant η_{liq} = 1 mPa·s and GLR = 0.3, 0.5, and 0.7, with varying GLO (left); the same measurements plotted over the entire gas momentum flow J_{gas} (see eq 8) (right).

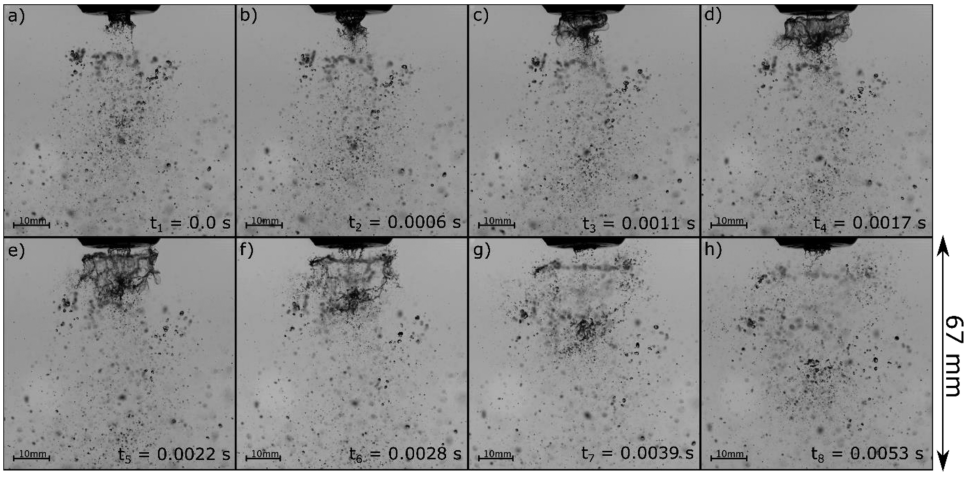

Figure 8. Primary breakup of the liquid sheet while pulsating at GLO = GLI applying nozzle configuration (iii), GLR = 0.3, and constant η_{liq} = 1 mPa·s. The time difference shown is respective to t_1.

Starting with a constant GLR = 0.3 shown in Figure 7 (left), for an increase in GLO (i.e., $v_{gas,o}$), which also leads to a decrease in GLI (i.e., $v_{gas,i}$), first between GLO = 0−0.06, the $ID_{32,m}$ remains near 130 μm. For further increase in GLO = 0.12−0.18, a steep increase in the $ID_{32,m}$ values can be noted, resulting in a maximum for GLO = 0.18. A further increase in GLO, up to GLO = 0.3, leads to a decrease in $ID_{32,m}$, even below the size at GLI = 0.3. These results are in accordance with those of Zhao et al.,[29] namely, the resulting droplet size primarily depends on the gas flow featuring higher velocity applying configuration (iii). For GLR = 0.5, the values for $ID_{32,m}$ remain lower compared to those for GLR = 0.3 through all the investigated GLOs. Increasing GLR from 0.5 to 0.7 only leads to a slight decrease in the droplet size. When GLR is increased from 0.5 to 0.7, the maximum in $ID_{32,m}$ around GLO ≈ GLI no longer exists. Both the mentioned effects can be explained by the aerodynamic force of the gas phase. The decreasing influence of GLR on the droplet size for increasing GLR was already shown and explained in Figure 3 (right). In order to understand the development of a maximum in the

https://doi.org/10.1021/acs.iecr.1c01526
Ind. Eng. Chem. Res. 2021, 60, 11502−11512

resulting droplet size, Figure 7 (right) presents the $ID_{32,m}$ values plotted as a function of the total emerging gas momentum flow. Here, a significant decrease in the latter was identified around the operating conditions of GLO ≈ GLI, which was caused by the comparably low velocity of both the emerging gas streams.

In addition, the HSC images taken at GLO ≈ GLI show a pulsation of the liquid sheet for all the investigated GLR values. As the frequency of the pulsation increases with increasing GLR, a time lapse of the pulsation with the HSC images could be detected best at GLR = 0.3, as shown in Figure 8. In Figure 8a, the liquid sheet was formed, as typical for nozzles in configurations (ii) or (iii). After Δt = 0.0011 s, the liquid sheet swelled, as shown in Figure 8c. At t_5 = 0.0022 s, the interaction of the swelled sheet with the high-velocity outer gas flow resulted in a detachment from the nozzle. As the swelled sheet was moved in the axial direction, large membranes were formed with a thick horizontal rim. After the rupture of the sheet at t_8 = 0.0053 s, the pulsation process began again with a new liquid sheet formed at the nozzle orifice. Because of the fact that the membrane rim falls apart into large droplets at low gas momentum flow, the droplet size at GLO ≈ GLI was increased for GLR < 0.7 compared to the operational conditions where GLO ≠ GLI.

The description of the disintegration process of the liquid sheet at GLO ≈ GLI for nozzle configuration (iii) can be given in accordance with the study by Zhao et al.[29] Here, it was assumed that the liquid sheet was disintegrated by Kelvin−Helmholtz instabilities, which formed a horizontal wave on the outer and inner sides of the sheet. This instability is caused by changes in the local static pressure, which is induced by differences in gas- and liquid-phase velocities.[41,42] The frequency f_{KH} and velocity u_c of these instabilities were defined by Villermaux et al.[43] and Dimotakis et al.,[44] according to eqs 11 and 12:

$$f_{KH} \sim \frac{u_c}{\delta_{gas}} \times \left(\frac{\rho_{gas}}{\rho_{liq}}\right)^{0.5} \tag{11}$$

$$u_c = \frac{\sqrt{\rho_{liq}} \times v_{liq}}{\sqrt{\rho_{liq}} + \sqrt{\rho_{gas}}} + \frac{\sqrt{\rho_{gas}} \times v_{gas}}{\sqrt{\rho_{liq}} + \sqrt{\rho_{gas}}} \tag{12}$$

Here, δ_{gas} stands for the gas boundary layer thickness. As the frequency, the gas boundary layer thickness, and the velocity of the instability were mainly the functions of gas velocity, these values were nearly equal for GLO ≈ GLI ($v_{gas,o} \approx v_{gas,i}$). In the event that the Kelvin−Helmholtz waves from both shear layers (inside and outside) emerged at the same time, the pulsation of the primary breakup was achieved and remains stable because of the comparable wave frequency and velocity. Furthermore, the increase in the instability frequency for increasing GLR values also corresponds to eq 12.

4.2.2. Influence of GLO/GLI on the Droplet Size and Primary Breakup Applying Nozzle Configuration (iii) at Varying Liquid Viscosities and Constant GLR = 0.5. In order to compare the primary breakup and droplet size applying nozzle configuration (iii) at constant GLR = 0.5, but varying GLO and GLI, as well as dynamic viscosity, the measurements specified in Table 4 were also performed for η_{liq} = 100 mPa·s. For η_{liq} = 200 and 400 mPa·s, a reduced measurement matrix at GLR = 0.5 with GLO = 0, 0.25, and 0.5 was conducted, the results of which are shown in Figure 9.

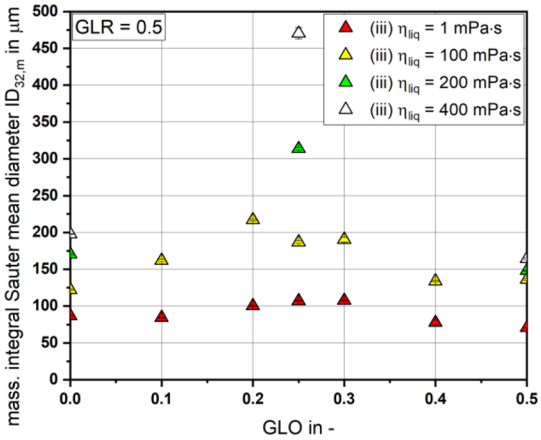

Figure 9. $ID_{32,m}$ measurements applying nozzle configuration (iii) at constant GLR = 0.5 with varying GLO and varying η_{liq} = 1 − 400 mPa·s.

As the dynamic viscosity of the liquid was increased from η_{liq} = 1 to 100 mPa·s, an increase in the droplet size was detected over the entire range of GLO. At GLO = 0, an increment in dynamic viscosity was observed, with $\Delta ID_{32,m}$ = 36 μm and the smallest effect on the $ID_{32,m}$ value. An even more pronounced maximum in the $ID_{32,m}$ value was also found at an increased viscosity, again in the region of GLO ≈ GLI ($v_{gas,o} \approx v_{gas,i}$). A further increase in dynamic viscosity to η_{liq} = 200−400 mPa·s led to higher $ID_{32,m}$ values for all GLO values. The smallest gradient in the droplet size for a further increase in viscosity was found at GLO = 0.5. The maximum of $ID_{32,m}$ at GLO ≈ GLI ($v_{gas,o} \approx v_{gas,i}$) showed a significant enlargement at viscosities of η_{liq} = 200−400 mPa·s. In order to explain these results, HSC images from the primary sheet breakup at GLO = 0, 0.25, and 0.5 are shown for η_{liq} = 400 mPa·s in Figure 10.

As already noted in the description of Figure 6d, upon applying configuration (ii) at GLR = 0.5 and η_{liq} = 400 mPa·s, almost no ligaments occur after the primary breakup because of the direct disintegration of the liquid sheet into droplets. When GLO is changed from GLO = 0 to GLO = 0.25, the pulsation described in Figure 8 can be detected, and it is even more pronounced for increased viscosity (see Figure 10b). Based on the significant damping effects of the liquid at η_{liq} = 400 mPa·s compared to η_{liq} = 1 mPa·s, the pulsation frequency of the liquid sheet is reduced with increased viscosity. The detachment of the liquid sheet, also shown in Figure 8 c for η_{liq} = 1 mPa·s, at higher viscosity, results in a large quantity of blown-up membranes. After the pulsation process with the membrane disintegration, large parts of the membrane rim slowly move in the axial direction. As the number density of the droplets at GLO ≈ GLI ($v_{gas,o} \approx v_{gas,i}$) is low and contains large liquid rim fragments because of the lower aerodynamic forces of the gas jets, the $ID_{32,m}$ values shown in Figure 9 are significantly increased. A further increase to GLO = 0.5 results in a maximum of the spray angle, as depicted in Figure 10c. This increased spray angle can be seen for all viscosities ≥100 mPa·s at GLO = 0.5. The increment in the spray angle can be explained by Kelvin−Helmholtz instabilities, which develop on the liquid sheet as a result of shear forces between the fast gas and slower liquid stream. As the liquid accumulation disintegrates, the local pressure difference generates a radial velocity compound and results in this spray angle. The trend, that for GLO = 0.5 the smallest $ID_{32,m}$ value at η_{liq} = 400 mPa·s

https://doi.org/10.1021/acs.iecr.1c01526
Ind. Eng. Chem. Res. 2021, 60, 11502−11512

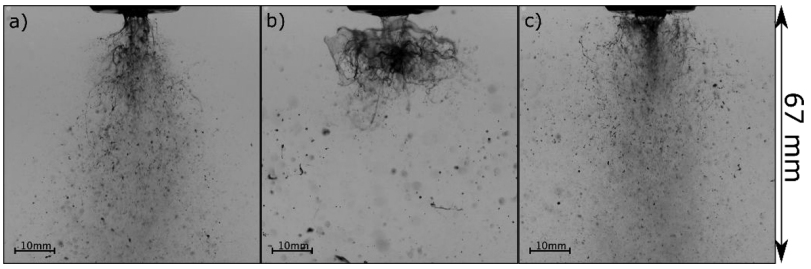

Figure 10. Primary breakup of the liquid sheet applying nozzle configuration (iii), GLR = 0.5, and constant η_{liq} = 400 mPa·s at (a) GLO = 0; (b) GLO = 0.25; and (c) GLO = 0.5.

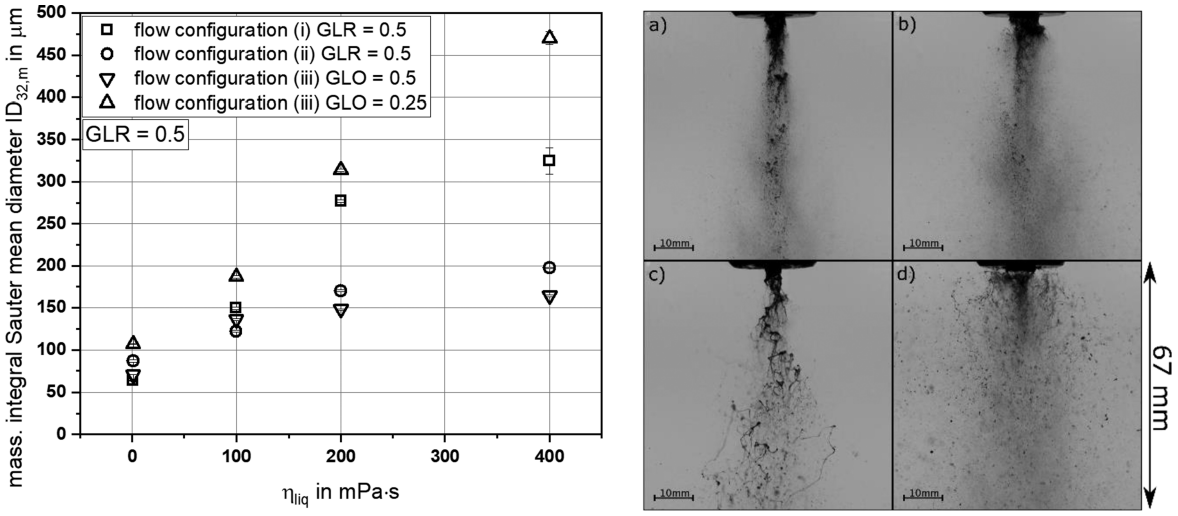

Figure 11. $ID_{32,m}$ measurements at constant GLR = 0.5 and varying η_{liq} = 1−400 mPa·s for nozzle configurations (i), (ii), and (iii) at GLO = 0.25 and (iii) GLO = 0.5 (left); primary breakup applying GLR = 0.5 for (a) configuration (i) and η_{liq} = 1 mPa·s; (b) configuration (iii) at GLO = 0.5 and η_{liq} = 1 mPa·s; (c) configuration (i) and η_{liq} = 400 mPa·s; and (d) configuration (iii) at GLO = 0.5 and η_{liq} = 400 mPa·s (right).

was detected compared to GLO = 0 and 0.25, is also apparent in the high-speed images.

4.3. Comparison of Nozzle Configurations (i), (ii), and (iii) at Constant GLR = 0.5. For the comparison of the applied nozzle configurations at constant GLR = 0.5 and varying liquid viscosity, four different setups were chosen: central liquid jet configuration (i), central gas jet configuration (ii) (the same as configuration (iii) at GLO = 0), nozzle configuration (iii) at GLO = 0.25, and configuration (iii) at GLO = 0.5. The resulting $ID_{32,m}$ values of the measurements are shown in Figure 11 (left). Figure 11 (right) presents the primary breakup at GLR = 0.5, applying two nozzle configurations (i) and (iii) at GLO = 0.5 with two viscosities η_{liq} = 1 and 400 mPa·s.

As already discussed in the previous section, for all of the nozzle configurations with increasing liquid viscosity, an increase in the droplet size was detected. The resulting droplet size exhibits a distinct dependence on the nozzle configuration used. As the variation in the resulting droplet size is $\Delta ID_{32,m}$ = 45 μm at η_{liq} = 1 mPa·s, the difference at η_{liq} = 400 mPa·s is calculated as $\Delta ID_{32,m}$ = 315 μm. For nozzle configuration (iii) at GLO = 0.25, the highest droplet size was detected at each applied dynamic viscosity. This was in accordance with the comparably low gas momentum flow and the trend toward the pulsation of the liquid sheet, as discussed in the previous chapters. Although the central liquid jet configuration (i) showed the smallest values in $ID_{32,m}$ at η_{liq} = 1 mPa·s, a significant increase in the droplet size was detected at higher viscosities. The increment in the droplet size at high viscosities results from the relation between the thickness of the primary ligament (d_{inner} = 5.4 mm) and the damping effects of the viscosity. Following primary atomization, ligaments and fragments are formed out of the jet, which leads to large droplets. Nozzle configurations (ii) at GLR = 0.5 and (iii) at GLO = 0.5 indicated the smallest gradient in the droplet size for increasing the dynamic viscosity, which could be explained by the high gas momentum flow in conjunction with the disintegration of a thin liquid sheet of s_1 = 1.09 mm. The lowest $ID_{32,m}$ value at increased viscosity was achieved by configuration (iii) at GLO = 0.5.

As configuration (iii) at GLO = 0.5 and configuration (i) at GLR = 0.5 are both designs with inner liquid discharge and a fast surrounding gas jet [(i) is the central liquid jet with the surrounding gas jet and (iii) at GLO = 0.5 is a liquid sheet with the surrounding gas jet], the difference in the resulting droplet size was also related to the difference in the liquid jet/sheet thickness. This significant difference is also shown in Figure 11 (right). The comparison of the flow configurations (i)−(iii) revealed, especially for increased liquid viscosities ($\eta_{liq} \geq$ 100 mPa s), a more efficient atomization for the sheet configurations (ii) and (iii) in relation to the jet configuration (i).

With reference to the literature review and the predominating gas stream applying configuration (iii), previous studies showed, depending on atomization conditions, that either the inner or the outer gas stream can be more relevant for

https://doi.org/10.1021/acs.iecr.1c01526
Ind. Eng. Chem. Res. 2021, 60, 11502−11512

atomization and sheet disintegration. In the present case of constant momentum flow ratios at GLO = 0.5 (GLI = 0) compared to GLI = 0.5 (GLO = 0), the outer high-velocity gas stream led to smaller droplets and thus was more relevant for atomization.

5. CONCLUSIONS

This study compares three different nozzle flow configurations: a central liquid jet with the surrounding gas phase, a liquid sheet with the central gas phase, and a liquid sheet with inner and outer gas phases. To guarantee constant velocities, as well as momentum flows at the nozzle orifice, one nozzle with identical orifice areas (a central tube with inner and outer slits) was utilized in the experiments. The influence of gas velocity (GLR), dynamic viscosity of the liquid, and nozzle configuration on the resulting droplet sizes (D_{32}, $ID_{32,m}$) and primary breakup was investigated at a constant liquid mass flow of $\dot{M}_{liq}$ = 30 kg·h^{-1}. On the basis of these findings, the following conclusions can be drawn:

- An increase in the gas momentum flow always resulted in a decrease in the droplet size for all flow configurations.
- An increase in dynamic viscosity always led to an increase in the resulting droplet size for all flow configurations and gas momentum flows.
- Comparing the flow configurations, the liquid sheet (ii and iii) revealed smaller droplet sizes against the liquid jet configuration (i).
- Operating the sheet nozzle in configuration (iii) with identical gas velocity for the inner and outer gas streams, pulsation of the liquid sheet was detected. Increasing the gas velocity (inner and outer) resulted in an increase in the pulsation frequency, leading to a reduced number of ligaments. Higher liquid viscosity resulted in the formation of large ligaments.
- In contrast to the literature, no dominant effect of the central gas jet compared to the outer gas stream was identified. Instead, the outer gas momentum flow seems to be more effective in terms of droplet size, especially when atomizing high-viscosity liquids.

AUTHOR INFORMATION

Corresponding Author

Simon Wachter − *Institute for Technical Chemistry, Karlsruhe Institute of Technology, 76344 Eggenstein-Leopoldshafen, Germany;* orcid.org/0000-0001-8264-8246; Email: simon.wachter@kit.edu

Authors

Tobias Jakobs − *Institute for Technical Chemistry, Karlsruhe Institute of Technology, 76344 Eggenstein-Leopoldshafen, Germany*

Thomas Kolb − *Institute for Technical Chemistry, Karlsruhe Institute of Technology, 76344 Eggenstein-Leopoldshafen, Germany; Engler-Bunte Institute, Karlsruhe Institute of Technology, 76131 Karlsruhe, Germany*

Complete contact information is available at: https://pubs.acs.org/10.1021/acs.iecr.1c01526

Notes

The authors declare no competing financial interest.

ACKNOWLEDGMENTS

The authors gratefully acknowledge the financial support of the Helmholtz Association of German Research Centers (HGF) in the context of the research program as well as Materials and Technologies for the Energy Transition (MTET). The present work contributes to the Helmholtz Virtual Institute for Gasification Technology − HVIGasTech (VH-VI-429) (http://www.hvigastech.org/).

REFERENCES

(1) Chigier, N.; Faragó, Z. Morphological Classification of Disintegration of Round Liquid Jets in a Coaxial Air Stream. *Atomiz. Spr.* **1992**, *2*, 137−153.

(2) Lasheras, J. C.; Hopfinger, E. J. Liquid jet instability and atomization in a coaxial gas stream. *Annu. Rev. Fluid Mech.* **2000**, *32*, 275−308.

(3) Zhao, H.; Hou, Y.-B.; Liu, H.-F.; Tian, X.-S.; Xu, J.-L.; Li, W.-F.; Liu, Y.; Wu, F.-Y.; Zhang, J.; Lin, K.-F. Influence of rheological properties on air-blast atomization of coal water slurry. *J. Non-Newton. Fluid Mech.* **2014**, *211*, 1−15.

(4) Rizk, N. K.; Lefebvre, A. H. Spray characteristics of plain-jet airblast atomizers. *Amer. Soc. Mech. Engineer.* **1984**, *106*, 634−638.

(5) Jakobs, T.; Djordjevic, N.; Sänger, A.; Zarzalis, N.; Kolb, T. Influence of reactor pressure on twin-fluid atomization: Basic investigations on burner design for high-pressure entrained flow gasifier. *Atomiz. Spr.* **2015**, *25*, 1081−1105.

(6) Wittig, S.; Aigner, M.; Sakbani, K.; Sattelmayer, T. *Optical Measurements of Droplet Size Distributions: Special Considerations in the Parameter Definition for Fuel Atomizers*; In AGARD Combust. Probl. in Turbine Eng., 1984.

(7) Elkotb, M.M.; El-Sayed Mahdy, M.A.; Montaser, M.E. *Investigation of external mixing air blast atomizers*; International Conference on Liquid Atomization and Spray Systems (ICLASS), 1982.

(8) Jasuja, A. K. Plain-Jet Airblast Atomization of Alternative Liquid Petroleum Fuels Under High Ambient Air Pressure Conditions. *Amer. Soc. Mech. Engineer.* **1982**, 7.

(9) Wachter, S.; Jakobs, T.; Kolb, T. Experimental investigation on the influence of system pressure on resulting spray quality and jet breakup applying pressure adapted twin-fluid nozzles. *Int. J. Multiphase Flow* **2020**, *125*, 103189.

(10) Lorenzetto, G. E.; Lefebvre, A. H. Measurements of drop size on a plain-jet airblast atomizer. *AIAA Journal* **1977**, *15*, 1006−1010.

(11) Schmidt, P.; Walzel, P. Zerstäuben von Flüssigkeiten. *Chem. Ing. Tech.* **1980**, *52*, 304−311.

(12) Aliseda, A.; Hopfinger, E. J.; Lasheras, J. C.; Kremer, D. M.; Berchielli, A.; Connolly, E. K. Atomization of viscous and non-Newtonian liquids by a coaxial, high-speed gas jet. Experiments and droplet size modeling. *Int. J. Multiphase Flow* **2008**, *34*, 161−175.

(13) Li, L. K. B.; Dressler, D. M.; Green, S. I.; Davy, M. H. Experiments on air-blast atomization of viscoelastic liquids, Part 1: quiescent conditions. *Atomiz. Spr.* **2009**, *19*, 157−190.

(14) Sänger, A.; Jakobs, T.; Kolb, T. *Using Primary Instability Analysis for Determination of Apparent Liquid Viscosity at Jet Breakup Atomizing Non-Newtonian Fluids*. 27th Annual Conference on Liquid Atomization and Spray Systems, 2016.

(15) Leboucher, N.; Roger, F.; Carreau, J.-L. Characteristics of the spray produced by the atomization of an annular liquid sheet assisted by an inner gas jet. *Atomiz. Spr.* **2012**, *22*, 515−542.

(16) Zhao, H.; Xu, J.-L.; Wu, J.-H.; Li, W.-F.; Liu, H.-F. Breakup morphology of annular liquid sheet with an inner round air stream. *Chem. Eng. Sci.* **2015**, *137*, 412−422.

(17) Kendall, J. M. Experiments on annular liquid jet instability and on the formation of liquid shells. *Phys. Fluids* **1986**, *29*, 2086.

(18) Choi, C. J.; Lee, S. Y. Droplet formation from a thin hollow liquid jet with a core air flow. *Atomiz. Spr.* **2005**, *15*, 469−488.

(19) Li, X.; Shen, J. Experimental Study of Sprays from Annular Liquid Jet Breakup. *J. Propul. Power* **1999**, *15*, 103−110.

(20) Carvalho, I. S.; Heitor, M. V. Liquid film break-up in a model of a prefilming airblast nozzle. *Exp. Fluids* **1998**, *24*, 408−415.
(21) Wahono, S.; Honnery, D.; Soria, J.; Ghojel, J. High-speed visualisation of primary break-up of an annular liquid sheet. *Exp. Fluids* **2008**, *44*, 451−459.
(22) Duke, D.; Honnery, D.; Soria, J. Experimental investigation of nonlinear instabilities in annular liquid sheets. *J. Fluid Mech.* **2012**, *691*, 594−604.
(23) Duke, D.; Honnery, D.; Soria, J. The growth of instabilities in annular liquid sheets. *Exp. Therm. Fluid Sci.* **2015**, *68*, 89−99.
(24) Cao, J. Theoretical and experimental study of atomization from an annular liquid sheet. *Proc. Instit. Mech. Eng., Part D: J. Automob. Engineer.* **2005**, *217*, 735−743.
(25) Ibrahim, A. A.; Jog, M. A. Nonlinear instability of an annular liquid sheet exposed to gas flow. *Int. J. Multiphase Flow* **2008**, *34*, 647−664.
(26) LEE, J.-G.; CHEN, L.-D. Linear stability analysis of gas-liquid interface. *AIAA Journal* **1991**, *29*, 1589−1595.
(27) Duke, D.; Honnery, D.; Soria, J. *Empirical Scaling Analysis of Atomising Annular Liquid Sheets*; International Conference of Liquid Atomization and Spray Systems (ICLASS), 2012.
(28) Leboucher, N.; Roger, F.; Carreau, J. L. Atomization characteristics of an annular liquid sheet with inner and outer gas flows. *Atomiz. Spr.* **2014**, *24*, 1065−1088.
(29) Zhao, H.; Wu, Z.-W.; Li, W.-F.; Xu, J.-L.; Liu, H.-F. Nonmonotonic Effects of Aerodynamic Force on Droplet Size of Prefilming Air-Blast Atomization. *Ind. Eng. Chem. Res.* **2018**, *57*, 1726−1732.
(30) Wachter, S.; Jakobs, T.; Kolb, T. Effect of Solid Particles on Droplet Size Applying the Time-Shift Method for Spray Investigation. *Appl. Sci.* **2020**, *10*, 7615.
(31) Tian, X.-S.; Zhao, H.; Liu, H.-F.; Li, W.-F.; Xu, J.-L. Effect of central tube thickness on wave frequency of coaxial liquid jet. *Fuel Process. Technol.* **2014**, *119*, 190−197.
(32) Searle, G.F.C. *A simple viscometer for very viscous liquids*; Proc. Cambridge Philos. Soc., 1912.
(33) Du Noüy, P. L. An Interfacial Tensiometer For Universal Use. *J. Gen. Physiol.* **1925**, *7*, 625−631.
(34) Wachter, S.; Jakobs, T.; Kolb, T. *Comparison of spray quality for two different flow configurations: Central liquid jet versus annular liquid sheet*; 29th European Conference on Liquid Atomization and Spray Systems (ILASS) 2019.
(35) Wachter, S.; Jakobs, T.; Kolb, T. Towards system pressure scaling of gas assisted coaxial burner nozzles − An empirical model. *Applicat. Energ. Comb. Sci.* **2021**, *5*, 100019.
(36) Araneo, L.; Damaschke, N.; Tropea, C. Measurement and Prediction of the Gaussian Beam Effect in the PDA. *Laser Techniq.Fluid Mech.* **2002**, 189−207.
(37) Kapulla, R.; Najera, S. B. Operation conditions of a phase Doppler anemometer: droplet size measurements with laser beam power, photomultiplier voltage, signal gain and signal-to-noise ratio as parameters. *Meas. Sci. Technol.* **2006**, *17*, 221−227.
(38) Albrecht, H.-E. *Laser doppler and phase doppler measurement techniques*; Springer: Berlin, New York, 2003.
(39) Schäfer, W.; Rosenkranz, S.; Brinckmann, F.; Tropea, C. Analysis of pneumatic atomizer spray profiles. *Particuology* **2016**, *29*, 80−85.
(40) DIN SPEC 91325:2015−06. *Charakterisierung von Sprays und Sprühprozessen durch die Messung der Größe und der Geschwindigkeit nicht-transparenter Tropfen; Text Deutsch und Englisch*; Beuth Verlag GmbH: Berlin, 2015.
(41) Helmholtz. XLIII. On discontinuous movements of fluids. *London, Edinburgh Dublin Philos. Mag. J. Sci.* **1868**, *36*, 337−346.
(42) Thomson, W. XLVI. Hydrokinetic solutions and observations. *London, Edinburgh Dublin Philos. Mag. J. Sci.* **1871**, *42*, 362−377.
(43) Marmottant, P.; Villermaux, E. On spray formation. *J. Fluid Mech.* **2004**, 73−111.
(44) Dimotakis, P. E. Two-dimensional shear-layer entrainment. *AIAA Journal* **1986**, *24*, 1791−1796.

https://doi.org/10.1021/acs.iecr.1c01526
Ind. Eng. Chem. Res. 2021, 60, 11502−11512